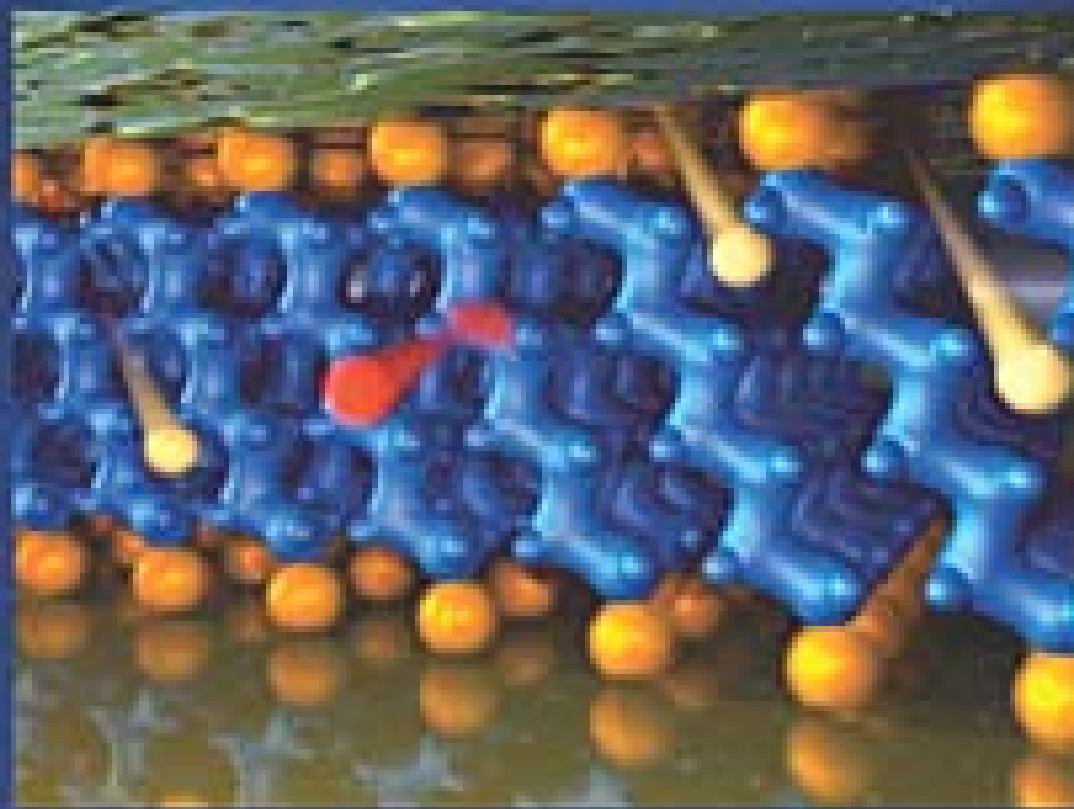


VOLUME 100  
 DECEMBER 2, 2004  
 NUMBER 48  
<http://pubs.acs.org/JPCB>

# THE JOURNAL OF PHYSICAL CHEMISTRY

# B

*Electric and Inelastic  
 Scattering in Alkane  
 Self-Assembled  
 Monolayers*  
 (see page 1879)



CONDENSED MATTER, MATERIALS, SURFACES, INTERFACES, & BIOPHYSICAL CHEMISTRY

PUBLISHED WEEKLY BY THE AMERICAN CHEMICAL SOCIETY



## FEATURE ARTICLE

## Elastic and Inelastic Electron Tunneling in Alkane Self-Assembled Monolayers

Wenyong Wang, Takhee Lee,<sup>†</sup> and Mark A. Reed\**Departments of Electrical Engineering, Applied Physics, and Physics, Yale University, P.O. Box 208284, New Haven, Connecticut 06520**Received: March 11, 2004; In Final Form: June 1, 2004*

A review of the mechanisms and characterization methods of molecular electronic transport is presented. Using self-assembled monolayers (SAMs) of alkanethiols in a nanometer-scale device structure, tunneling is unambiguously demonstrated to be the main conduction mechanism for large band gap SAMs exhibiting well-known temperature and length dependencies. Inelastic electron tunneling spectroscopy exhibits clear vibrational modes of the molecules in the device, presenting the first direct evidence of the presence of molecules in a molecular transport device and confirming the tunneling transport mechanism in alkane self-assembled monolayers.

## 1. Introduction

The suggestion<sup>1</sup> and demonstration<sup>2</sup> of using molecules as the active region of electronic devices has recently generated considerable interest in both the basic transport physics and potential technological applications of molecular electronics.<sup>3,4</sup> However some reports of molecular mechanisms in electronic devices<sup>5,6</sup> have been shown to be premature and due to filamentary conduction,<sup>7</sup> highlighting the fabrication sensitivity of molecular structures and the need to institute reliable controls and methods to validate true molecular transport.<sup>8</sup> A related problem is the characterization of molecules in the active device structure, including their configuration, bonding, and indeed even their very presence. Here we present results for well-understood molecular assemblies that exhibit understood classical transport behavior and can be used as a control for eliminating (or understanding) fabrication variables. Utilizing tunneling spectroscopic methods, we present the first unambiguous evidence of the presence of molecules in the junction and further confirm the charge-transport mechanism obtained by standard current–voltage characterizations.

A molecular system whose structure and configuration are sufficiently well characterized such that it can serve as a standard is the extensively studied alkanethiol ( $\text{CH}_3(\text{CH}_2)_{n-1}\text{SH}$ ) self-assembled monolayer (SAM).<sup>9</sup> This system is useful as a control because properly prepared SAMs form single van der Waals crystals,<sup>9,10</sup> and it presents a simple classical metal–insulator–metal (M–I–M) tunnel junction when fabricated between metallic contacts because of the large HOMO–LUMO gap (HOMO: highest occupied molecular orbital, LUMO: lowest unoccupied molecular orbital) of approximately 8 eV.<sup>11–13</sup>

Various surface analytical tools have been used to investigate the surface and bulk properties of the alkanethiol SAMs, such

as X-ray photoelectron spectroscopy,<sup>14</sup> Fourier transform infrared spectroscopy (FTIR),<sup>15</sup> Raman spectroscopy,<sup>16</sup> scanning tunneling microscopy (STM),<sup>10</sup> and so forth. Studies have shown that the bonding of the thiolate group to the gold surface is strong with a bonding energy of  $\sim 1.7$  eV.<sup>9</sup> STM topography examinations revealed that alkanethiols adopt the commensurate crystalline lattice characterized by a  $c(4 \times 2)$  superlattice of a  $(\sqrt{3} \times \sqrt{3})R30^\circ$ .<sup>10,17</sup> FTIR investigation showed that the orientation of the alkanethiol SAMs on Au(111) surfaces is tilted  $\sim 30^\circ$  from the surface normal.<sup>18</sup>

Electronic transport through alkanethiol SAMs has also been characterized by STM,<sup>19,20</sup> conducting atomic force microscopy,<sup>21–24</sup> mercury-drop junctions,<sup>25–28</sup> cross-wire junctions,<sup>29</sup> and electrochemical methods.<sup>30–32</sup> These investigations are exclusively at ambient temperature, clearly useful but insufficient for an unambiguous claim that the transport mechanism is tunneling (which is, of course, expected assuming that the Fermi levels of the contacts lie within the large HOMO–LUMO gap). However, in the absence of temperature-dependent current–voltage ( $I(V, T)$ ) characteristics, other conduction mechanisms (such as thermionic, hopping, or filamentary conduction) cannot be excluded and complicate the analysis, and thus such a claim is premature.

Utilizing a nanometer-scale device structure that incorporates alkanethiol SAMs, we demonstrate devices that allow  $I(V, T)$  and structure-dependent measurements<sup>33,34</sup> with results that can be compared with accepted theoretical models of M–I–M tunneling. The use of this fabrication approach is not special in any way (other than that we have so far found it to be successful); indeed we stress that any successful device fabrication method should yield the results described below if one is characterizing the intrinsic molecular transport properties.

Electronic transport is further investigated with the technique of inelastic electron tunneling spectroscopy (IETS).<sup>34</sup> IETS was developed in the 1960s as a powerful spectroscopic tool for the study of the vibrational spectrum of organic molecules confined inside metal–oxide–metal junctions.<sup>35–39</sup> In our study,

\* To whom correspondence should be addressed. E-mail: mark.reed@yale.edu.

<sup>†</sup> Current address: Department of Materials Science and Engineering, Gwangju Institute of Science and Technology, Gwangju 500-712, Korea.

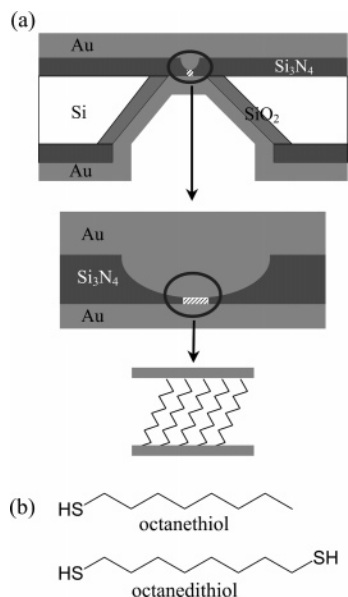


**Figure 1.** Schematics of a nanometer-scale device used in this study (not drawn to scale in relative thickness). (a) The top schematic is the cross section of a silicon wafer with a nanometer-scale pore etched through a suspended silicon nitride membrane. Middle and bottom schematics show a Au–SAM–Au junction formed in the pore area. (b) Structures of octanethiol and octanedithiol shown as examples.

IETS is used for the purpose of molecule identification and chemical bonding and conduction mechanism investigations of the “control” SAMs. The exclusive presence of well-known vibrational modes of the alkanes that are used is direct evidence of the molecules in the device structure, something that has to date only been inferred (with good reason, but nonetheless not unambiguously). The vibrational modes, exclusively identified as alkanes (as well as contact modes), are difficult to interpret in any way other than as components in the active region of the device. The inelastic tunneling spectra also demonstrate that electronic tunneling occurs through the molecules, confirming the conduction mechanism obtained by  $I(V, T)$  characterizations. The specific spectral lines also yield intrinsic line widths that may give insight into molecular conformation and may prove to be a powerful tool in future molecular device characterization.

## 2. Experiment

Electronic transport measurements on alkanethiol SAMs were performed using a device structure similar to one reported previously.<sup>33,34,40–42</sup> In this device, as illustrated in Figure 1a (not drawn to scale in relative thickness), a number of molecules (ca. several thousands) are sandwiched between two metallic contacts. This technique provides a stable device structure and makes cryogenic measurements possible. Device fabrication starts with a high-resistivity silicon wafer with a low-stress  $\text{Si}_3\text{N}_4$  film deposited on both sides by low-pressure chemical vapor deposition (LPCVD). By standard photolithography processing, a suspended  $\text{Si}_3\text{N}_4$  membrane ( $40 \mu\text{m} \times 40 \mu\text{m}$  size and  $\sim 70$  nm thickness) is fabricated on the top side of the wafer. Subsequent e-beam lithography and reactive ion etching create a single pore with a diameter of tens of nanometers through the membrane. As the next step, 150 nm gold is thermally evaporated onto the top side of the wafer to fill the pore and form one of the metallic contacts.

The device is then transferred to a molecular solution to deposit the SAM layer. For our experiments, a  $\sim 5$  mM alkanethiol solution is prepared by adding  $\sim 10 \mu\text{L}$  of alkanethiols to 10 mL of ethanol.<sup>43</sup> The deposition is done in solution

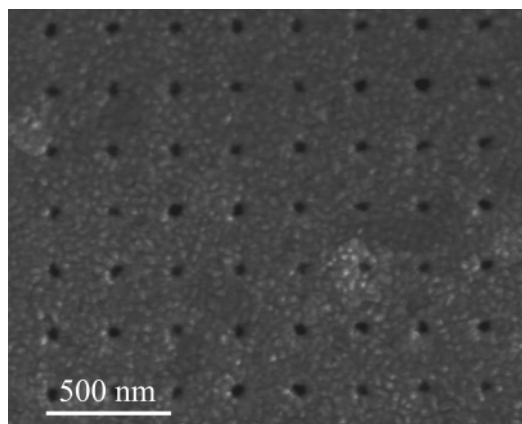


**Figure 2.** Scanning electron microscope image of a representative array of pores used to calibrate the device size. The scale bar is 500 nm.

for 24 h inside a nitrogen-filled glovebox with an oxygen level of less than 100 ppm. Three alkanemonothiol molecules of different molecular lengths—octanethiol ( $\text{CH}_3(\text{CH}_2)_7\text{SH}$ ; denoted as C8 for the number of alkyl units), dodecanethiol ( $\text{CH}_3(\text{CH}_2)_{11}\text{SH}$ , denoted as C12), and hexadecanethiol ( $\text{CH}_3(\text{CH}_2)_{15}\text{SH}$ , denoted as C16)—and one alkanedithiol molecule—octanedithiol ( $\text{HS}(\text{CH}_2)_8\text{SH}$ , denoted as C8-dithiol)—were used to form the active molecular components.<sup>43</sup> As representative examples, the chemical structures of octanethiol and octanedithiol are shown in Figure 1b.

To determine the pore size statistically, test patterns (arrays of pores) were created under similar fabrication conditions. Figure 2 shows a scanning electron microscope (SEM) image of such test pattern arrays. This indirect measurement of device size is done because an SEM examination of the actual device can cause hydrocarbon contamination of the device and subsequent contamination of the monolayer. From a regression analysis of 298 pores, the device sizes of the C8, C12, C16, and C8-dithiol samples are determined as  $50 \pm 8$ ,  $45 \pm 2$ ,  $45 \pm 2$ , and  $51 \pm 5$  nm in diameter, respectively. A more ideal (less parasitic) C8 sample supercedes that of previous reports,<sup>33</sup> and derived parameters from the two data sets agree to within standard error. We will use these device areas as the effective contact areas. Although one could postulate that the actual area of metal that contacts the molecules may be different, there is little reason to propose that it would be different as a function of length over the range of alkanethiols used, and at most it would be a constant systematic error.

The sample is then transferred under ambient conditions to an evaporator that has a cooling stage to deposit the opposing Au contact. During the thermal evaporation (under a pressure of  $\sim 10^{-8}$  Torr), liquid nitrogen is kept flowing through the cooling stage to avoid thermal damage to the molecular layer.<sup>33,44</sup> This technique reduces the kinetic energy of evaporated Au atoms at the surface of the monolayer, thus preventing Au atoms from punching through the monolayer. For the same reason, the evaporation rate is kept very low. For the first 10 nm of gold evaporated, the rate is less than  $0.1 \text{ \AA/s}$ . Then the rate is increased slowly to  $0.5 \text{ \AA/s}$  for the rest of the evaporation, and a total of 200 nm of gold is deposited to form the contact.

The device is subsequently packaged and loaded into a low-temperature cryostat. The sample temperature is varied from 300 to 4.2 K by flowing cryogen vapor onto the sample (and thermometer) using a closed-loop temperature controller. Two-terminal dc  $I(V)$  measurements are performed using a semiconductor parameter analyzer. Inelastic electron tunneling spectra are obtained via a standard lock-in second-harmonic

**TABLE 1: Possible Conduction Mechanisms<sup>a</sup>**

conduction mechanism	characteristic behavior	temperature dependence	voltage dependence
direct tunneling <sup>b</sup>	$J \approx V \exp\left(-\frac{2d}{\hbar}\sqrt{2m\Phi}\right)$	none	$J \approx V$
Fowler–Nordheim tunneling	$J \approx V^2 \exp\left(-\frac{4d\sqrt{2m\Phi^{3/2}}}{3q\hbar V}\right)$	none	$\ln\left(\frac{J}{V^2}\right) \approx \frac{1}{V}$
thermionic emission	$J \approx T^2 \exp\left(-\frac{\Phi - q\sqrt{qV/4\pi\epsilon d}}{k_B T}\right)$	$\ln\left(\frac{J}{T^2}\right) \approx \frac{1}{T}$	$\ln(J) \approx V^{1/2}$
hopping conduction	$J \approx V \exp\left(-\frac{\Phi}{k_B T}\right)$	$\ln\left(\frac{J}{V}\right) \approx \frac{1}{T}$	$J \approx V$

<sup>a</sup> Adapted from ref 46. <sup>b</sup> This characteristic of direct tunneling is valid for the low-bias regime; see eq 3a.

measurement technique.<sup>35,36</sup> A synthesized function generator is used to provide both the modulation and the lock-in reference signal. The second-harmonic signal (proportional to  $d^2I/dV^2$ ) is directly measured using a lock-in amplifier, which is checked to be consistent with a numerical derivative of the first-harmonic signal (proportional to  $dI/dV$ ). Various modulation amplitudes and frequencies are used to obtain the spectra. The ac modulation is added to a dc bias using operational amplifier-based custom circuitry.<sup>45</sup>

### 3. Theoretical Basis

**3.1. Possible Conduction Mechanisms.** In Table 1, possible conduction mechanisms are listed with their characteristic current, temperature, and voltage dependencies<sup>46</sup> (We do not discuss filamentary tunneling mechanisms, which are easier to categorize.<sup>47</sup>) On the basis of whether thermal activation is involved, the conduction mechanisms fall into two distinct categories: (i) thermionic or hopping conduction, which has temperature-dependent  $I(V)$  behavior and (ii) direct tunneling or Fowler–Nordheim tunneling, which does not have temperature-dependent  $I(V)$  behavior. For example, both thermionic and hopping conduction have been observed for 4-thioacetyl-biphenyl SAMs<sup>40</sup> and 1,4-phenylene diisocyanide SAMs.<sup>41b</sup> However, the conduction mechanism is expected to be tunneling when the Fermi levels of contacts lie within the large HOMO–LUMO gap for short molecules, as for the case of an alkanethiol molecular system.<sup>11–13</sup> Previous work on Langmuir–Blodgett alkane monolayers<sup>48</sup> exhibited a significant impurity-dominated transport component, complicating the analysis.  $I(V)$  measurements on self-assembled alkanethiol monolayers have also been reported;<sup>19–29,49</sup> however, all of these measurements were performed at a fixed temperature (300 K) that is insufficient for proving tunneling to be the dominant mechanism.

**3.2. Tunneling Models.** To describe the transport through a molecular system having HOMO and LUMO energy levels, one of the applicable models is the Franz two-band model.<sup>50–53</sup> This model provides a nonparabolic energy–momentum  $E(k)$  dispersion relationship by considering the contributions of both the HOMO and LUMO energy levels.<sup>50</sup>

$$k^2 = \frac{2m^*}{\hbar^2} E \left(1 + \frac{E}{E_g}\right) \quad (1)$$

where  $k$  is the imaginary part of the wave vector of electrons,  $m^*$  is the electron effective mass,  $h (= 2\pi\hbar)$  is Planck's constant,  $E$  is the electron energy, and  $E_g$  is the HOMO–LUMO energy gap. From this nonparabolic  $E(k)$  relationship, the effective mass of the electron tunneling through the SAM can be deduced by knowing the barrier height of the metal–SAM–metal junction.

When the Fermi level of the metal is aligned closely enough to one energy level (either HOMO or LUMO), the effect of the other distant energy level on the tunneling transport is negligible, and the widely used Simmons model<sup>54</sup> is an excellent approximation.<sup>55</sup> The Simmons model expresses the tunneling current density through a barrier in the tunneling regime of  $V < \Phi_B/e$  as<sup>25,54</sup>

$$J = \left(\frac{e}{4\pi^2\hbar d^2}\right) \left\{ \left(\Phi_B - \frac{eV}{2}\right) \exp\left[-\frac{2(2m)^{1/2}}{\hbar} \alpha \left(\Phi_B - \frac{eV}{2}\right)^{1/2} d\right] - \left(\Phi_B + \frac{eV}{2}\right) \exp\left[-\frac{2(2m)^{1/2}}{\hbar} \alpha \left(\Phi_B + \frac{eV}{2}\right)^{1/2} d\right] \right\} \quad (2)$$

where  $m$  is the electron mass,  $d$  is the barrier width,  $\Phi_B$  is the barrier height, and  $V$  is the applied bias. For molecular systems, the Simmons model has been modified with a parameter  $\alpha$ .<sup>25,33</sup>  $\alpha$  is a unitless adjustable parameter that is introduced to provide either a way of applying the tunneling model of a rectangular barrier to tunneling through a nonrectangular barrier<sup>25</sup> or an adjustment to account for the effective mass ( $m^*$ ) of the tunneling electrons through a rectangular barrier<sup>25,33,53,56</sup> or both.  $\alpha = 1$  corresponds to the case for a rectangular barrier and bare electron mass. By fitting individual  $I(V)$  data using eq 2,  $\Phi_B$  and  $\alpha$  values can be obtained.

Equation 2 can be approximated in two limits: low bias and high bias as compared with the barrier height  $\Phi_B$ . For the low-bias range, eq 2 can be approximated as<sup>54</sup>

$$J \approx \left(\frac{2m\Phi_B^{1/2} e^2 \alpha}{\hbar^2 d}\right) V \exp\left[-\frac{2(2m)^{1/2}}{\hbar} \alpha (\Phi_B)^{1/2} d\right] \quad (3a)$$

To determine the high-bias limit, we compare the relative magnitudes of the first and second exponential terms in eq 2. At high bias, the first term is dominant, and thus the current density can be approximated as

$$J \approx \left(\frac{e}{4\pi^2\hbar d^2}\right) \left(\Phi_B - \frac{eV}{2}\right) \exp\left[-\frac{2(2m)^{1/2}}{\hbar} \alpha \left(\Phi_B - \frac{eV}{2}\right)^{1/2} d\right] \quad (3b)$$

The tunneling currents in both bias regimes are exponentially dependent on the barrier width  $d$ . In the low-bias regime, the tunneling current density is

$$J \propto \frac{1}{d} \exp(-\beta_0 d)$$

where  $\beta_0$  is a bias-independent decay coefficient

$$\beta_0 = \frac{2(2m)^{1/2}}{\hbar} \alpha (\Phi_B)^{1/2} \quad (4a)$$

whereas in the high-bias regime

$$J \propto \frac{1}{d^2} \exp(-\beta_V d)$$

where  $\beta_V$  is a bias-dependent decay coefficient

$$\beta_V = \frac{2(2m)^{1/2}}{\hbar} \alpha \left( \Phi_B - \frac{eV}{2} \right)^{1/2} = \beta_0 \left( 1 - \frac{eV}{2\Phi_B} \right)^{1/2} \quad (4b)$$

At high bias,  $\beta_V$  decreases as bias increases, which results from a barrier lowering effect due to the applied bias.

## 4. Results

**4.1. Tunneling Current–Voltage Characteristics. Temperature–Variable Current–Voltage ( $I(V, T)$ ) Measurement.** To determine the conduction mechanism of self-assembled alkanethiol molecular systems,  $I(V)$  measurements over a sufficiently wide temperature range (300 to 80 K) and resolution (10 K) were performed. Figure 3a shows a representative  $I(V, T)$  characteristic of dodecanethiol (C12) measured with the device structure as shown in Figure 1a. Positive bias corresponds to electrons injected from the physisorbed Au contact (bottom contact in Figure 1a) into the molecules. By using the contact area of  $45 \pm 2$  nm in diameter determined from the SEM study, a current density of  $1500 \pm 200$  A/cm<sup>2</sup> at 1.0 V is determined. No significant temperature dependence of the characteristics (from  $V = 0$  to 1.0 V) is observed over the range from 300 to 80 K. An Arrhenius plot ( $\ln(I)$  versus  $1/T$ ) of this is shown in Figure 3b, exhibiting little temperature dependence in the slopes of  $\ln(I)$  versus  $1/T$  at different bias and thus indicating the absence of thermal activation. Therefore, we conclude that the conduction mechanism through alkanethiol is tunneling, contingent on demonstrating a correct molecular length dependence. The tunneling through alkanethiol SAMs has been assumed to be “through-bond” tunneling (i.e., along the tilted molecular chains between the metal contacts<sup>22,23,32,57</sup>). On the basis of the applied bias as compared with the barrier height ( $\Phi_B$ ), the tunneling through a SAM layer can be categorized into either direct ( $V < \Phi_B/e$ ) or Fowler–Nordheim ( $V > \Phi_B/e$ ) tunneling. These two tunneling mechanisms can be distinguished by their distinct voltage dependencies (Table 1). An analysis of  $\ln(I/V^2)$  versus  $1/V$  (in Figure 3c) shows no significant voltage dependence, indicating no obvious Fowler–Nordheim transport behavior in this bias range (0 to 1.0 V) and thus determining that the barrier height is larger than the applied bias (i.e.,  $\Phi_B > 1.0$  eV). This study is restricted to applied biases  $\leq 1.0$  V, and the transition from direct to Fowler–Nordheim tunneling requires higher bias. Having established tunneling as the conduction mechanism, we can now obtain the barrier height by comparing our experimental  $I(V)$  data with theoretical calculations from the aforementioned tunneling models.

**Tunneling Characteristics through Alkanethiols.** From the modified Simmons model (eq 2) by adjusting two parameters  $\Phi_B$  and  $\alpha$ , a nonlinear least-squares fitting can be performed to fit the measured C12  $I(V)$  data (calculation assuming  $\alpha = 1$  has been previously shown not to fit  $I(V)$  data well for some alkanethiol measurements at fixed temperature (300 K)).<sup>25</sup> By using a device size of 45 nm in diameter, the best fitting

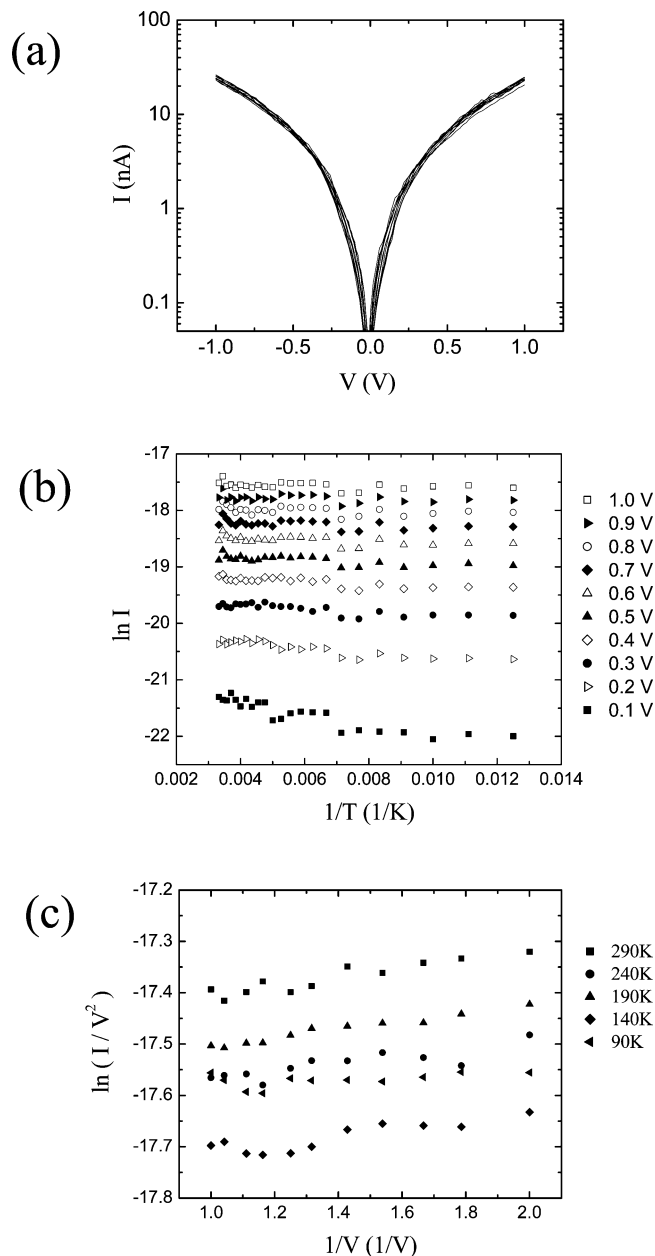


**Figure 3.** (a) Temperature-dependent  $I(V)$  characteristics of dodecanethiol (C12).  $I(V)$  data at temperatures from 300 to 80 K with 20 K steps are plotted on a log scale. (b) Arrhenius plot generated from the  $I(V)$  data in plot a from 0.1 to 1.0 V with 0.1 V steps. (c) Plot of  $\ln(I/V^2)$  versus  $1/V$  at selected temperatures.

parameters (minimizing  $\chi^2$ ) for the room-temperature C12  $I(V)$  data were found to be  $\Phi_B = 1.42 \pm 0.04$  eV and  $\alpha = 0.65 \pm 0.01$ , where the error ranges of  $\Phi_B$  and  $\alpha$  are dominated by potential device-size fluctuations of 2 nm. Likewise, data sets were obtained and fittings were done for octanethiol (C8) and hexadecanethiol (C16), which yielded values of  $\{\Phi_B = 1.83 \pm 0.10$  eV and  $\alpha = 0.61 \pm 0.01\}$  and  $\{\Phi_B = 1.40 \pm 0.03$  eV,  $\alpha = 0.68 \pm 0.01\}$ , respectively.

Using  $\Phi_B = 1.42$  eV and  $\alpha = 0.65$ , a calculated  $I(V)$  for C12 is plotted as a solid curve on a linear scale (Figure 4a) and on a semilog scale (Figure 4b). A calculated  $I(V)$  for  $\alpha = 1$  and  $\Phi_B = 0.65$  eV (which gives the best fit in the low-bias range) is shown as the dashed curve in the same Figure, illustrating that with  $\alpha = 1$  only limited regions of the  $I(V)$  can be fit (specifically here for  $V < 0.3$  V). For the case of a rectangular barrier, the  $\alpha$  parameter fit presented above corresponds to an effective mass  $m^*$  ( $= \alpha^2 m$ ) of 0.42  $m$ .

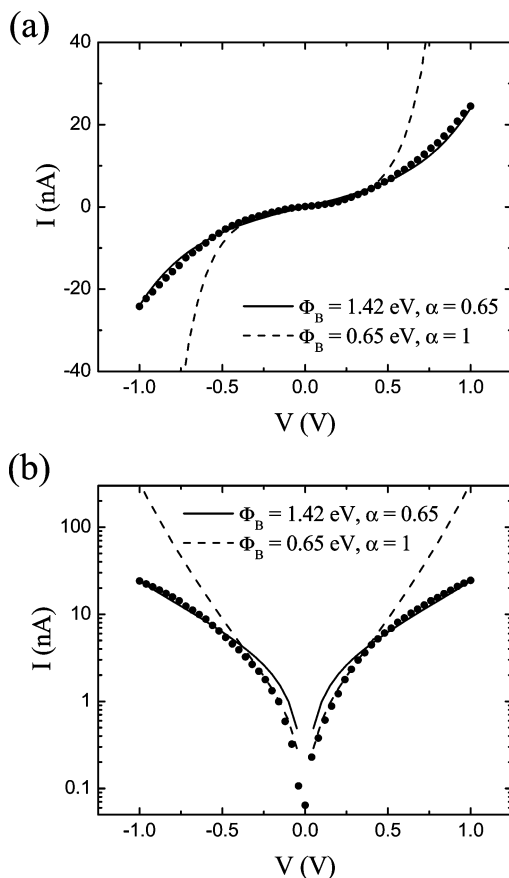


**Figure 4.** Measured C12  $I(V)$  data (●) compared with the calculation (—) using the optimum fitting parameters of  $\Phi_B = 1.42$  eV and  $\alpha = 0.65$ . The calculated  $I(V)$  from a simple rectangular model ( $\alpha = 1$ ) with  $\Phi_B = 0.65$  eV is also shown as the dashed curve. Current is plotted (a) on a linear scale and (b) on a log scale.

To investigate the dependency of the Simmons model fitting on  $\Phi_B$  and  $\alpha$ , a fitting minimization analysis was undertaken for the individual  $\Phi_B$  and  $\alpha$  values as well as their product form of  $\alpha\Phi_B^{1/2}$  in eq 4a.  $\Delta(\Phi_B, \alpha) = (\sum |I_{\text{expt},V} - I_{\text{calcd},V}|^2)^{1/2}$  was calculated and plotted, where  $I_{\text{expt},V}$  represents the experimental current–voltage values and  $I_{\text{calcd},V}$  is calculated using eq 2. Different  $\{\Phi_B, \alpha\}$  pairs (7500) were used in the fittings with  $\Phi_B$  ranging from 1.0 to 2.5 eV (0.01 eV increment) and  $\alpha$  ranging from 0.5 to 1.0 (0.01 increment). Figure 5a is a representative contour plot of  $\Delta(\Phi_B, \alpha)$  versus  $\Phi_B$  and  $\alpha$  values generated for the C12  $I(V)$  data, where darker regions correspond to smaller  $\Delta(\Phi_B, \alpha)$  and various shades represent half-order of magnitude  $\Delta(\Phi_B, \alpha)$  steps. The darker regions represent better fits of eq 2 to the measured  $I(V)$  data. In the inset of Figure 5a, one can see that there are a range of possible  $\Phi_B$  and  $\alpha$  values yielding minimum fitting parameters. Although the tunneling parameters determined from the previous Simmons tunneling fitting  $\{\Phi_B = 1.42$  eV and  $\alpha = 0.65\}$  lie within this minimum region in this Figure, there is a distribution of other possible values.

A plot of  $\Delta(\Phi_B, \alpha)$  versus  $\alpha\Phi_B^{1/2}$  for the same device reveals a more pronounced dependence and is shown in Figure 5b. This plot indicates that the fitting to the Simmons model sharply depends on the product of  $\alpha\Phi_B^{1/2}$ . For this plot,  $\Delta(\Phi_B, \alpha)$  is minimized at a  $\alpha\Phi_B^{1/2}$  of  $0.77$  (eV) $^{1/2}$  corresponding to a  $\beta_0$  value of  $0.79$  Å $^{-1}$  from eq 4a. The C8 and C16 devices showed similar results, indicating that the Simmons tunneling model has a strong  $\alpha\Phi_B^{1/2}$  dependence. For the C8 device, although the  $\Phi_B$  obtained from the fitting is a little larger, combined  $\alpha$

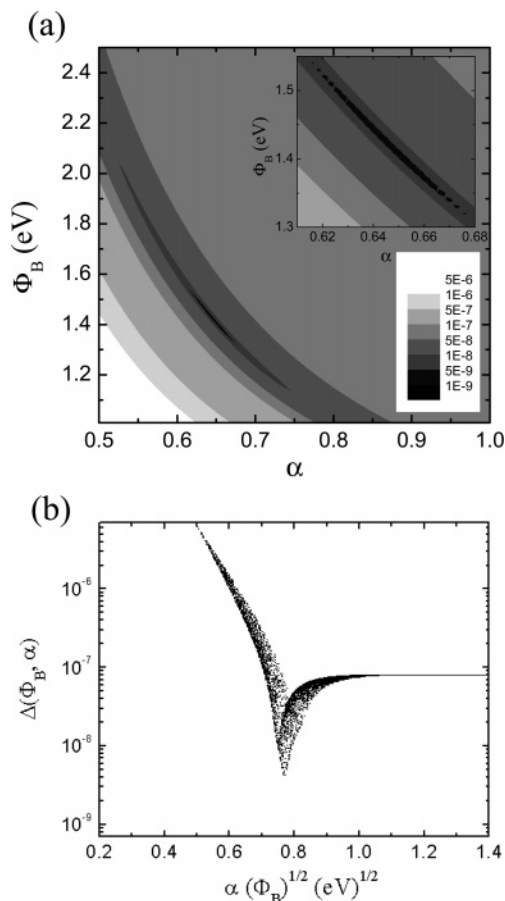


**Figure 5.** (a) Contour plot of  $\Delta(\Phi_B, \alpha)$  values for the C12 nanopore device as a function of  $\Phi_B$  and  $\alpha$ , where the darker region corresponds to a better fit. The inset shows detailed minimization fitting regions. (b) Plot of  $\Delta(\Phi_B, \alpha)$  as a function of  $\alpha\Phi_B^{1/2}$ .

and  $\Phi_B$  gives a similar  $\beta_0$  value within the error range as the C12 and C16 devices (Table 2).

**Length-Dependent Tunneling through Alkanethiols.** Three alkanethiols of different molecular length, C8, C12, and C16, were investigated to study length-dependent tunneling behavior. Figure 6 is a semilog plot of tunneling current densities multiplied by molecular length ( $Jd$  at low bias and  $Jd^2$  at high bias) as a function of the molecular length for these alkanethiols. The molecular lengths used in this plot are 13.3, 18.2, and 23.2 Å for C8, C12, and C16, respectively. Each molecular length was determined by adding an Au–thiol bonding length to the length of the molecule.<sup>22</sup> Note that these lengths assume through-bond tunneling.<sup>22,23,32,57</sup> The high- and low-bias regimes are defined somewhat arbitrarily by comparing the relative magnitudes of the first and second exponential terms in eq 2. Using  $\Phi_B = 1.42$  eV and  $\alpha = 0.65$  obtained from nonlinear least-squares fitting of the C12  $I(V)$  data, the second term becomes less than  $\sim 10\%$  of the first term at  $\sim 0.5$  V, which is chosen as the boundary of low- and high-bias ranges.

As seen in Figure 6, the tunneling current shows an exponential dependence on molecular length, which is consistent with the Simmons tunneling model (eq 3). The  $\beta$  values can be determined from the slope at each bias and are plotted in Figure 7. The error bar of an individual  $\beta$  value in this plot was obtained by considering both the device size uncertainties and the linear fitting errors.

The determined  $\beta$  values are almost independent of bias in the low-bias range ( $V \lesssim 0.5$  V), and an average  $\beta$  of  $0.77 \pm 0.06$  Å $^{-1}$  in this region (from 0 to 0.5 V) can be calculated

**TABLE 2: Summary of Alkanethiol Tunneling Parameters in This Study**

molecules	$J$ at 1 V (A/cm <sup>2</sup> )	$\Phi_B$ (eV)	$\alpha$	$m^*$ (m)	$\beta_0$ (Å <sup>-1</sup> ) <sup>a</sup>
C8	31 000 ± 10 000	1.83 ± 0.10	0.61 ± 0.01	0.37	0.85 ± 0.04
C12	1500 ± 200	1.42 ± 0.04	0.65 ± 0.01	0.42	0.79 ± 0.02
C16	23 ± 2	1.40 ± 0.03	0.68 ± 0.01	0.46	0.82 ± 0.02
C8-dithiol	93 000 ± 18 000	1.20 ± 0.03	0.59 ± 0.01	0.35	0.66 ± 0.02

<sup>a</sup>  $\beta_0$  values were calculated using eq 4a.

**TABLE 3: Summary of Alkanethiol Tunneling Characteristic Parameters**

junction	$\beta^a$ (Å <sup>-1</sup> )	$J^b$ (A/cm <sup>2</sup> ) at 1 V	$\Phi_B$ (eV)	technique	ref
(bilayer) monothiol	0.87 ± 0.1	25–200 <sup>c</sup>	2.1 <sup>g</sup>	Hg junction	25
(bilayer) monothiol	0.71 ± 0.08	0.7–3.5 <sup>c</sup>		Hg junction	27
monothiol	0.79 ± 0.01	1500 ± 200 <sup>d</sup>	1.4 <sup>g</sup>	solid M–I–M	33
monothiol	1.2			STM	19
dithiol	0.8 ± 0.08	3.7–5 × 10 <sup>5e</sup>	5 ± 2 <sup>h</sup>	STM	20
monothiol	0.73–0.95	1100–1900 <sup>f</sup>	2.2 <sup>g</sup>	CAFM	21
monothiol	0.64–0.8	10–50 <sup>f</sup>	2.3 <sup>g</sup>	CAFM	23
dithiol	0.46 ± 0.02	3–6 × 10 <sup>5e</sup>	1.3–1.5 <sup>g</sup>	CAFM	24
monothiol	1.37 ± 0.03		1.8 <sup>h</sup>	tuning fork AFM	49
monothiol	0.97 ± 0.04			electrochemical	30
monothiol	0.85			electrochemical	31
monothiol	0.91 ± 0.08			electrochemical	32
monothiol	0.76	2 × 10 <sup>4</sup> (at 0.1 V) <sup>e</sup>	1.3–3.4 <sup>i</sup>	theory	58
monothiol	0.76			theory	59
monothiol	0.79			theory	56

<sup>a</sup> Some decay coefficients  $\beta$  were converted into the unit of Å<sup>-1</sup> from the unit of per methylene. <sup>b</sup> Current densities ( $J$ ) for C12 monothiol or dithiol at 1 V are extrapolated from published results for other length molecules by using conductance  $\propto \exp(-\beta d)$  relationship. <sup>c</sup> Junction area estimated by optical microscopy. <sup>d</sup> Junction area estimated by SEM. <sup>e</sup> Junction area estimated for a single molecule. <sup>f</sup> Junction area estimated by Hertzian contact theory. <sup>g</sup> Barrier height  $\Phi_B$  values obtained from the Simmons equation. <sup>h</sup> Barrier height  $\Phi_B$  values obtained from the bias dependence of  $\beta$ . <sup>i</sup> Barrier height  $\Phi_B$  values obtained from a theoretical calculation.

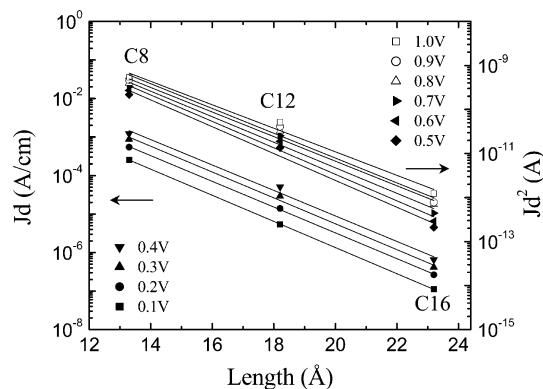


**Figure 6.** Log plot of tunneling current densities multiplied by molecular length  $d$  at low bias and by  $d^2$  at high bias (symbols) versus molecular length. The lines through the data points are linear fittings.

from Figure 7. Table 3 is a summary of previously reported alkanethiol transport parameters obtained by different techniques. The current densities ( $J$ ) listed in Table 3 are for C12 monothiol or dithiol devices at 1 V, which are extrapolated from published results of alkane molecules of other lengths. The large variation in  $J$  from these reports can be attributed to the uncertainties in device contact geometry and junction area as well as complicating inelastic or defect contributions. The  $\beta$  value ( $0.77 \pm 0.06 \text{ Å}^{-1} \approx 0.96 \pm 0.08$  per methylene) for alkanethiols reported here is comparable to previously reported values as summarized in Table 3. This  $\beta$  value agrees with the value of  $0.79 \text{ Å}^{-1}$  ( $\beta_0$ ) calculated via eq 4a from fitting individual  $I(V)$  characteristic of the C12 device. The calculated  $\beta_0$  values of C8 and C16 devices are similar, as summarized in Table 2.

According to eq 4b,  $\beta_V^2$  depends on bias  $V$  linearly in the high-bias range. The inset in Figure 7 is a plot of  $\beta_V^2$  versus  $V$  in this range (0.5 to 1.0 V) along with a linear fitting of the data. From this fitting,  $\Phi_B = 1.35 \pm 0.20 \text{ eV}$  and  $\alpha = 0.66 \pm$

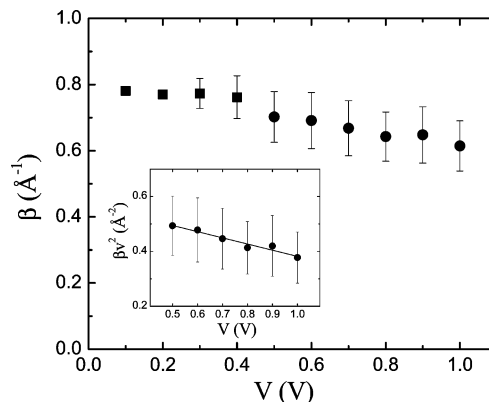


**Figure 7.** Plot of  $\beta$  versus bias in the low-bias range (■) and the high-bias range (●). The inset shows a plot of  $\beta_V^2$  versus bias with a linear fitting.

0.04 were obtained from the intercept and the slope, respectively, consistent with the values  $\{\Phi_B = 1.42 \text{ eV and } \alpha = 0.65\}$  obtained from the nonlinear least-squares fitting in the previous section.

$\beta$  values for alkanethiols obtained by various experimental techniques have previously been reported and are summarized in Table 3.<sup>19–33,49</sup> To compare with these reported  $\beta$  values, we also performed length-dependent analysis on our experimental data according to the generally used equation<sup>20–28,33</sup>

$$G = G_0 \exp(-\beta d) \quad (5)$$

This gives a  $\beta$  value from  $0.84$  to  $0.73 \text{ Å}^{-1}$  in the bias range from  $0.1$  to  $1.0 \text{ V}$ , which is comparable to results reported previously. For example, Holmlin et al. reported a  $\beta$  value of  $0.87 \text{ Å}^{-1}$  by mercury drop experiments,<sup>25</sup> Wold et al. reported a  $\beta$  of  $0.94 \text{ Å}^{-1}$ , and Cui et al. reported  $\beta$  of  $0.64 \text{ Å}^{-1}$  for various alkanethiols by using a conducting atomic force microscope

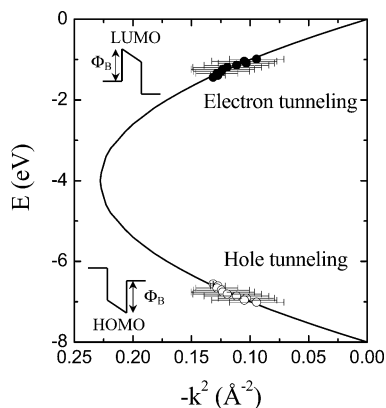


**Figure 8.**  $E(k)$  relationship (symbols) generated from the length-dependent measurement data for alkanethiols. Solid and open symbols correspond to electron and hole tunneling, respectively. The insets show the corresponding energy-band diagrams. The solid curve is the Franz two-band expression for  $m^* = 0.43m$ .

technique.<sup>21,23</sup> These reported  $\beta$  values were treated as bias-independent quantities, contrary to the results reported here and that observed in a slightly different alkane system (ligand-encapsulated nanoparticle/alkane–dithiol molecules).<sup>24</sup> We also caution against the use of parameters that have not been checked with a temperature-dependent analysis because small non-tunneling components can dramatically affect derived values of  $\beta$ .

**Franz Model.** We have analyzed our experimental data using a Franz two-band model.<sup>50–53</sup> Because there is no reliable experimental data on the Fermi level alignment in these metal–SAM–metal systems,  $\Phi_B$  and  $m^*$  are treated as adjustable parameters. We performed a least-squares fit on our data with the Franz nonparabolic  $E(k)$  relationship (eq 1) using an alkanethiol HOMO–LUMO gap of 8 eV.<sup>12,13</sup> Figure 8 shows the resultant  $E(k)$  relationship and the corresponding energy-band diagrams. The zero of energy in this plot was chosen as the LUMO energy. The best fitting parameters obtained by minimizing  $\chi^2$  were  $\Phi_B = 1.49 \pm 0.51$  eV and  $m^* = 0.43 \pm 0.15$  m, where the error ranges of  $\Phi_B$  and  $m^*$  are dominated by the error fluctuations of  $\beta$  [ $k^2 = -(\beta/2)^2$ ]. Both electron tunneling near the LUMO and hole tunneling near the HOMO can be described by these parameters.  $\Phi_B = 1.49$  eV indicates that the Fermi level is aligned near one energy level in either case; therefore, the Simmons model is a valid approximation. The  $\Phi_B$  and  $m^*$  values obtained here are in reasonable agreement with the previous results obtained from the Simmons model.

**4.2. Inelastic Tunneling, Inelastic Electron Tunneling Spectroscopy.** Electronic transport through alkanethiol SAMs is further investigated with the technique of inelastic electron tunneling spectroscopy,<sup>34</sup> such as in the 1966 work of Jaklevic and Lambe, who studied the conductance of tunnel junctions with encased organic molecules.<sup>35</sup> Since then, it has become a powerful spectroscopic tool for chemical identification, chemical bonding investigation, and surface chemistry and physics studies.<sup>38</sup> In an inelastic tunneling process, the electron loses energy to a localized vibrational mode with a frequency  $\nu$  when the applied bias satisfies the condition of  $eV = h\nu$ . As a result, an additional tunneling channel is opened for the electron, resulting in an increase in the total current at the applied bias corresponding to the vibrational-mode energy.<sup>37</sup> Typically, only a small fraction of tunneling electrons are involved in the inelastic tunneling process (determined by the electron–vibronic mode coupling coefficient), resulting in a small conductance change that is commonly measured in the second harmonics of

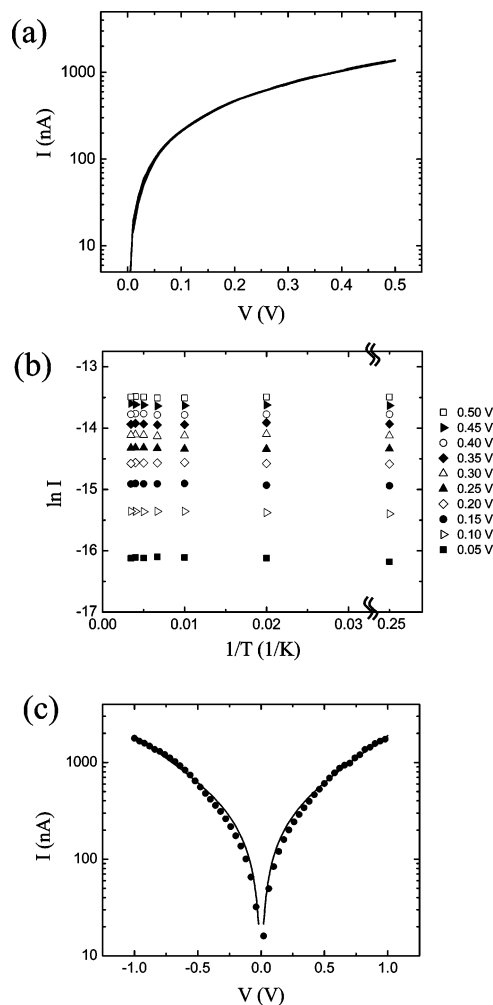


**Figure 9.** (a)  $I(V, T)$  characteristics of a C8-dithiol SAM at selected temperatures (4.2, 50, 100, 150, 200, 250, and 290 K). (b) Arrhenius plot generated from the data in plot a at voltages from 0.1 to 0.5 V with 0.05 V steps. (c) Measured C8-dithiol  $I(V)$  data at room temperature (●) is compared with the calculation (–) using the optimum fitting parameters of  $\Phi_B = 1.20$  eV and  $\alpha = 0.59$ .

a phase-sensitive detector that yields the characteristic frequencies of the corresponding vibrational modes as well as other information.<sup>36–38</sup>

$I(V, T)$  measurements and additional IETS studies have been performed on an octanedithiol (C8-dithiol) SAM using the aforementioned device structure shown in Figure 1a.<sup>34</sup> Figure 9a shows the  $I(V, T)$  data for this device obtained from 300 to 4.2 K. An Arrhenius plot shown in Figure 9b exhibits little temperature dependence, verifying that tunneling is the main transport mechanism for C8-dithiol SAMs. This result is in good agreement with the tunneling transport characteristics observed previously. Figure 9c shows the room-temperature  $I(V)$  measurement result. Using a junction area of  $51 \pm 5$  nm in diameter (obtained from statistical studies of the nanopore size with SEM), a current density of  $(9.3 \pm 1.8) \times 10^4$  A/cm<sup>2</sup> at 1.0 V is calculated. As a comparison, a current density of  $(3.1 \pm 1.0) \times 10^4$  A/cm<sup>2</sup> at 1.0 V was observed for C8-monothiol SAMs. Using the modified Simmons model (eq 2), we obtained transport parameters of  $\Phi_B = 1.20 \pm 0.03$  eV and  $\alpha = 0.59 \pm 0.01$  ( $m^* = 0.34m$ ) for this C8-dithiol SAM.

Figure 10 shows the IETS spectrum of the same C8-dithiol SAM device obtained at  $T = 4.2$  K. An ac modulation of 8.7 mV (rms value) at a frequency of 503 Hz was applied to the sample to acquire the second-harmonic signals. The spectra are

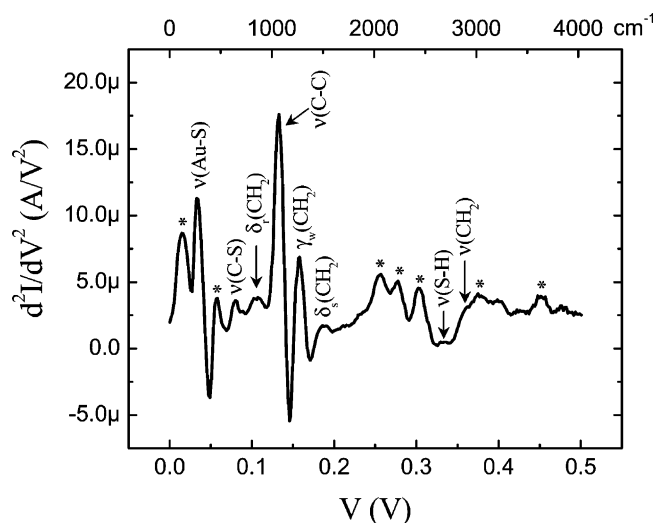


**Figure 10.** Inelastic electron tunneling spectrum of a C8-dithiol SAM obtained from lock-in second-harmonic measurement with an ac modulation of 8.7 mV (rms value) at a frequency of 503 Hz ( $T = 4.2$  K). Peaks labeled \* are most probably background due to the encasing  $\text{Si}_3\text{N}_4$ .

**TABLE 4: Summary<sup>a</sup> of the Major Vibrational Modes of Alkanethiolates<sup>b</sup>**

modes	methods	wavenumber ( $\text{cm}^{-1}$ )	(meV)
$\nu(\text{Au-S})$	HREELS <sup>61</sup>	225	28
$\nu(\text{C-S})$	Raman <sup>60</sup>	641	79
	Raman <sup>60</sup>	706	88
$\delta_{r,s}(\text{CH}_2)$	HREEL <sup>61</sup>	715	89
	IR <sup>62</sup>	720	89
	IR <sup>62</sup>	766	95
	IR <sup>62</sup>	925	115
$\nu(\text{C-C})$	HREEL <sup>61</sup>	1050	130
	Raman <sup>60</sup>	1064	132
	Raman <sup>60</sup>	1120	139
$\gamma_{w,l}(\text{CH}_2)$	IR <sup>62</sup>	1230	152
	HREELS <sup>61</sup>	1265	157
	IR <sup>62</sup>	1283	159
	IR <sup>62</sup>	1330	165
$\delta_s(\text{CH}_2)$	HREELS <sup>61</sup>	1455	180
$\nu(\text{S-H})$	Raman <sup>60</sup>	2575	319
$\nu_s(\text{CH}_2)$	Raman <sup>60</sup>	2854	354
	HREELS <sup>61</sup>	2860	355
$\nu_{as}(\text{CH}_2)$	Raman <sup>60</sup>	2880	357
	Raman <sup>60</sup>	2907	360
	HREELS <sup>61</sup>	2925	363

<sup>a</sup> There is a vast amount of literature with spectroscopic assignments for alkanethiols. The references given are representative of IR, Raman, and HREELS assignments. <sup>b</sup> Taken from refs 60–62.

stable and repeatable upon successive bias sweeps. The spectrum at 4.2 K is characterized by three pronounced peaks in the 0 to 200 mV region at 33, 133, and 158 mV. From comparison with previously reported infrared (IR), Raman, and high-resolution electron energy loss (HREEL) spectra of SAM-covered gold surfaces (Table 4), these three peaks are assigned to  $\nu(\text{Au-S})$ ,  $\nu(\text{C-C})$ , and  $\gamma_w(\text{CH}_2)$  modes of a surface-bound alkanethiolate.<sup>60–63</sup> The absence of a strong  $\nu(\text{S-H})$  signal at  $\sim 329$  mV suggests that most of the thiol groups have reacted with the gold bottom and top contacts. Peaks are also reproducibly observed at 80, 107, and 186 mV. They correspond to  $\nu(\text{C-S})$ ,  $\delta_{r,s}(\text{CH}_2)$ , and  $\delta_s(\text{CH}_2)$  modes. The stretching mode of the  $\text{CH}_2$  groups,  $\nu(\text{CH}_2)$ , appears as a shoulder at 357 meV. The peak at 15 mV is due to vibrations from either Si, Au, or  $\delta(\text{C-C})$

C).<sup>64</sup> We note that all alkanethiolate peaks without exception or omission occur in the spectra. Peaks at 58, 257, 277, and 302 as well as above 375 mV are likely to originate from Si–H and N–H vibrations related to the silicon nitride membrane,<sup>64a,65</sup> which forms the SAM encasement. To the best of our knowledge, alkanethiols have no vibrational signatures in these regions. Measurement of the background spectrum of an “empty” nanopore device with only gold contacts to obtain background contributions from  $\text{Si}_3\text{N}_4$  is hampered by currents that are either too low (open circuit) or too high (short circuit) in such a device. A similar IETS result has also recently been obtained using a different test structure.<sup>66</sup>

Although there are no selection rules in IETS as there are in IR and Raman spectroscopy, certain selection preferences have been established. According to IETS theory,<sup>67</sup> molecular vibrations with net dipole moments perpendicular to the interface of the tunneling junction have larger peak intensities than vibrations with net dipole moments parallel to the interface (for dipoles close to the electrodes). Thus, vibrations perpendicular to the electrode interface (i.e.,  $\nu(\text{Au-S})$ ,  $\nu(\text{C-S})$ ,  $\nu(\text{C-C})$ , and  $\gamma_w(\text{CH}_2)$ ) dominate the IETS spectrum, and modes parallel to the interface (i.e.,  $\delta_{r,s}(\text{CH}_2)$  and  $\nu(\text{CH}_2)$ ) are weak, as clearly shown in Figure 10.

**Line-Width Study.** To verify that the observed spectra are indeed valid IETS data, peak-width broadening was examined as a function of temperature and modulation voltage. IETS was performed with different ac modulations at a fixed temperature and at different temperatures with a fixed ac modulation. Figure 11a shows the modulation dependence of the IETS spectra obtained at 4.2 K, and Figure 11b shows the modulation broadening of the C–C stretching mode at 133 meV. The circular symbols are the full width at half-maximum (fwhm) values of the experimental peak at  $T = 4.2$  K with various modulation voltages. A Gaussian distribution function was utilized to obtain a fwhm and the error range.<sup>68</sup> The square symbols are calculated fwhm values ( $W_{\text{theoretical}}$ ) taking into account both a finite temperature effect ( $W_{\text{thermal}} \approx 5.4k_B T$ )<sup>36</sup> and a finite voltage modulation effect ( $W_{\text{modulation}} \approx 1.7V_{\text{ac,rms}}$ ).<sup>69</sup> These two broadening contributions add as the squares:  $W_{\text{theoretical}}^2 = W_{\text{thermal}}^2 + W_{\text{modulation}}^2$ . The agreement is excellent over most of the modulation range, but we note a saturation of the line width at low modulation bias indicating the influence of a nonnegligible intrinsic line width. Taking into account the known thermal and modulation broadenings and including the intrinsic line width ( $W_1$ )<sup>70</sup> as a fitting parameter, the measured peak width ( $W_{\text{exptl}}$ ) is given by

$$W_{\text{exptl}} = \sqrt{W_1^2 + W_{\text{thermal}}^2 + W_{\text{modulation}}^2} \quad (6)$$

$W_1$  can be determined by using a nonlinear least-squares fit to the ac modulation data (Figure 11) with eq 6, giving an intrinsic line width of  $3.73 \pm 0.98$  meV for this line. This is shown (with the error range) in Figure 11b as a shaded bar, including the thermal contribution.

We can independently check the thermal broadening of the line at fixed modulation width. Figure 12a shows the temperature dependence of the IETS spectra obtained with an ac modulation of 8.7 mV (rms value). In Figure 12b, the circular symbols (and corresponding error bars) are experimental fwhm values of the C–C stretching mode from Figure 12a, determined by a Gaussian fit (and error of the fit) to the experimental line shape. For simplicity, we have considered only Gaussian line shapes,<sup>68</sup> resulting in increased error bars for the lower-temperature range due to an asymmetric line shape. The square symbols are

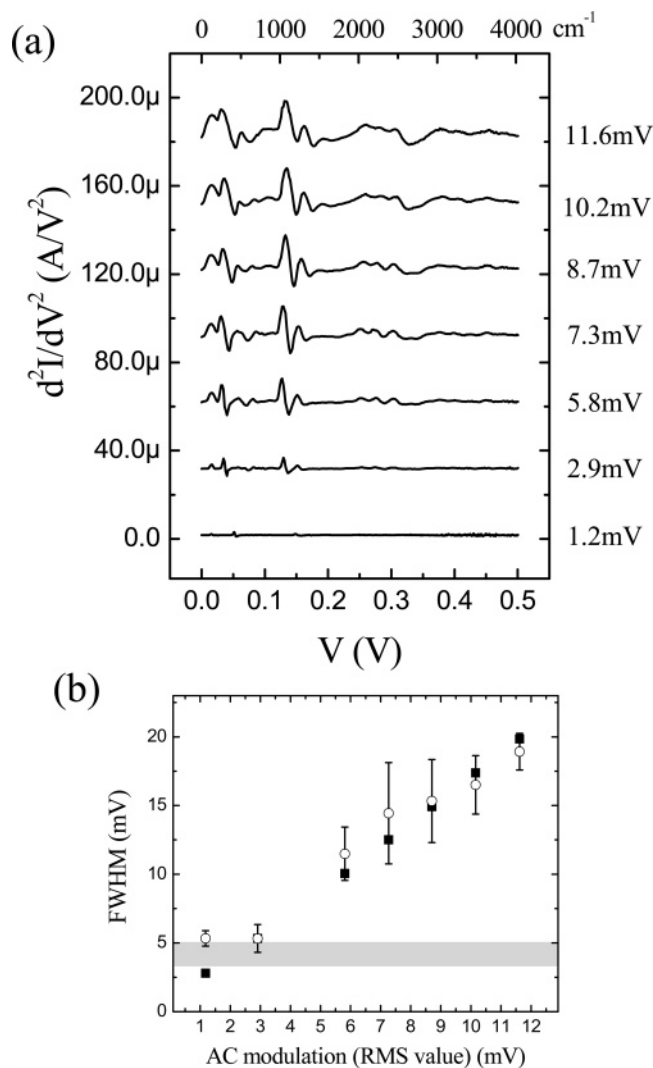


**Figure 11.** (a) Modulation dependence of IETS spectra obtained at 4.2 K. (b) Line (C–C stretching mode) broadening as a function of ac modulation. The circular symbols are experimental fwhm values, and the square symbols are theoretical calculations considering both modulation and thermal contributions. The shaded bar denotes the expected saturation due to the derived intrinsic line width (including a  $5.4k_B T$  thermal contribution) of  $3.73 \pm 0.98$  meV.

theoretical calculations considering thermal broadening, modulation broadening, and the intrinsic line width determined above. The error ranges of the calculation (due to the intrinsic line width error) are approximately the size of the data points. The agreement between theory and experiment is very good, spanning a temperature range from below ( $\times 0.5$ ) to above ( $\times 10$ ) the thermally broadened intrinsic line width. This line width should be a sensitive test to compare to theoretical models of transmission probabilities.<sup>71</sup>

## 5. Conclusions

We present here a study of electron tunneling through alkanethiol SAMs, with the intent that this system can serve as a simple control for the development of well-characterized molecular junctions. The characteristics are consistent with accepted models of M–I–M tunneling junctions and present a system on which tunneling spectroscopy can be performed.

The field of molecular electronics is rich in the proposal and promise of numerous device concepts<sup>72,73</sup> but unfortunately has an absence of reliable data and characterization techniques upon which to test these ideas. It is incumbent upon the experimental-

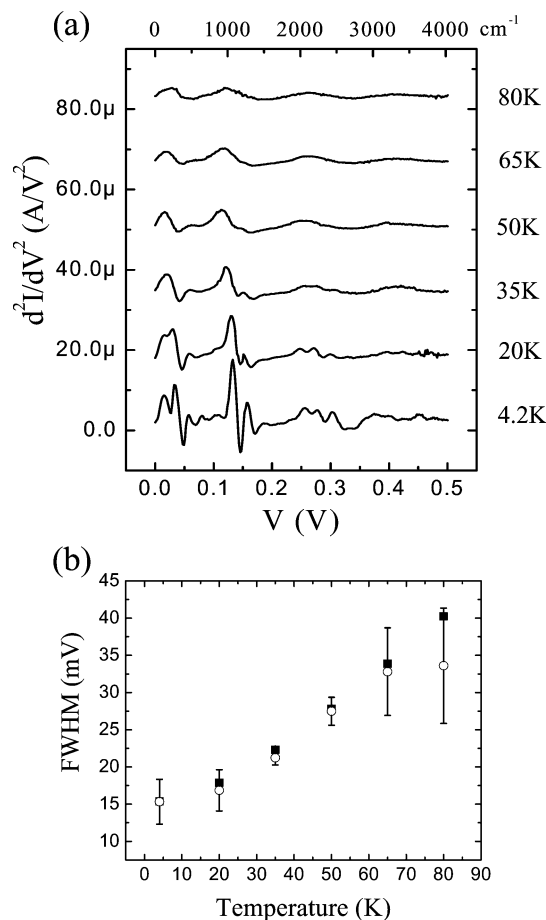


**Figure 12.** (a) Temperature dependence of IETS spectra obtained at a fixed ac modulation of 8.7 mV (rms value). (b) Line (C–C stretching mode) broadening as a function of temperature. The circular symbols are experimental fwhm values, and the square symbols are theoretical calculations considering thermal broadening, modulation broadening, and the intrinsic line width.

ist to institute controls carefully to validate claims of intrinsic molecular behavior. Systematic controls, such as the model system presented here, should assist in guiding further work toward a rational development of the fascinating device structures and systems that the field promises.

**Acknowledgment.** We thank J. F. Klemic, X. Li, and R. Munden for helpful discussions and assistance. We especially thank I. Kretzschmar for assistance in the peak identification of the IETS spectra. This work was supported by DARPA/ONR (N00014-01-1-0657), ARO (DAAD19-01-1-0592), AFOSR (F49620-01-1-0358), NSF (DMR-0095215), and NASA (NCC 2-1363).

**Note Added after ASAP Posting.** This article was posted ASAP on 7/30/2004. A data label in Figure 12 has been changed. The correct version was posted on 8/05/2004.

## References and Notes

- Reed, M. A.; Tour, J. M. *Sci. Am.* **2000**, June, 86–93.
- Reed, M. A.; Zhou, C.; Muller, C. J.; Burgin, T. P.; Tour, J. M. *Science* **1997**, *278*, 252–254.
- Molecular Nanoelectronics*; Reed, M. A., Lee, T., Eds.; American Scientific Publishers: Stevenson Ranch, CA, 2003.
- (a) Heath, J. R.; Ratner, M. A. *Phys. Today* **2003**, May, 43–49.
- (b) Nitzan, A.; Ratner, M. A. *Science* **2003**, *300*, 1384–1389.
- (a) Chen, Y.; Jung, G.-Y.; Ohlberg, D. A. A.; Li, X.; Stewart, D. R.; Jeppesen, J. O.; Nielsen, K. A.; Stoddart, J. F.; Williams, R. S. *Nanotechnology* **2003**, *14*, 462–468. (b) *Beyond Silicon: Breakthroughs*

in *Molecular Electronics*; <http://www.hpl.hp.com/research/qsr/> (Hewlett-Packard Quantum Science Research).

(6) (a) Luo, Y.; Collier, C. P.; Jeppesen, J. O.; Nielsen, K. A.; Delonno, E.; Ho, G.; Perkins, J.; Tseng, H.-R.; Yamamoto, T.; Stoddart, J. F.; Heath, J. R. *Chem. Phys. Chem.* **2002**, *3*, 519–525. (b) Collier, C. P.; Mattersteig, G.; Wong, E. W.; Luo, Y.; Beverly, K.; Sampaio, J.; Raymo, F. M.; Stoddart, J. F.; Heath, J. R. *Science* **2000**, *289*, 1172–1175.

(7) (a) Stewart, D. R.; Ohlberg, D. A. A.; Beck, P. A.; Chen, Y.; Williams, R. S.; Jeppesen, J. O.; Nielsen, K. A.; Stoddart, J. F. *Nano Lett.* **2004**, *4*, 133–136. (b) Lau, C. N.; Stewart, D. R.; Williams, R. S.; Bockrath, M. *Nano Lett.* **2004**, *4*, 569–572.

(8) Lee, T.; Wang, W.; Klemic, J. F.; Zhang, J. J.; Su, J.; Reed, M. A. *J. Phys. Chem. B* **2004**, *108*, 8742–8750.

(9) Ulman, A. *An Introduction to Ultrathin Organic Films from Langmuir–Blodgett to Self-Assembly*; Academic Press: Boston, 1991.

(10) Poirier, G. E. *Chem. Rev.* **1997**, *97*, 1117–1127.

(11) Ratner, M. A.; Davis, B.; Kemp, M.; Mujica, V.; Roitberg, A.; Yaliraki, S. In *Molecular Electronics: Science and Technology*; Aviram, A., Ratner, M., Eds.; Annals of the New York Academy of Sciences; New York Academy of Sciences: New York, 1998; Vol. 852.

(12) Although the HOMO–LUMO gap of alkyl chain-type molecules has been reported,<sup>13</sup> there is no experimental data on the HOMO–LUMO gap for the Au/alkanethiol SAM/Au system. A commonly used HOMO–LUMO gap for alkanethiol is 8 eV.

(13) (a) Boulas, C.; Davidovits, J. V.; Rondelez, F.; Vuillaume, D. *Phys. Rev. Lett.* **1996**, *76*, 4797–4800. (b) Fujihira, M.; Inokuchi, H. *Chem. Phys. Lett.* **1972**, *17*, 554–556. (c) Lias, S. G.; Bartmess, J. E.; Liebman, J. F.; Holmes, J. L.; Levin, R. D.; Mallard, W. G. *J. Phys. Chem. Ref. Data* **1998**, *17*, 24. (d) Yang, H.-H.; McCreery, R. L. *Anal. Chem.* **1999**, *71*, 4081.

(14) Walczak, M. W.; Chung, C.; Stole, S. M.; Widrig, C. A.; Porter, M. D. *J. Am. Chem. Soc.* **1991**, *113*, 2370–2378.

(15) Nuzzo, R. G.; Zegarski, B. R.; Dubois, L. H. *J. Am. Chem. Soc.* **1987**, *109*, 733–740.

(16) Widrig, C. A.; Chung, C.; Porter, M. D. *J. Electroanal. Chem.* **1991**, *310*, 335–359.

(17) Poirier, G. E.; Tarlov, M. J. *Langmuir* **1994**, *10*, 2853–2856.

(18) Porter, M. D.; Bright, T. B.; Allara, D. L.; Chidsey, C. E. D. *J. Am. Chem. Soc.* **1987**, *109*, 3559–3568.

(19) Bumm, L. A.; Arnold, J. J.; Dunbar, T. D.; Allara, D. L.; Weiss, P. S. *J. Phys. Chem. B* **1999**, *103*, 8122–8127.

(20) Xu, B.; Tao, N. J. *Science* **2003**, *301*, 1221–1223.

(21) Wold, D. J.; Frisbie, C. D. *J. Am. Chem. Soc.* **2001**, *123*, 5549–5556.

(22) Wold, D. J.; Haag, R.; Rampi, M. A.; Frisbie, C. D. *J. Phys. Chem. B* **2002**, *106*, 2813–2816.

(23) Cui, X. D.; Zaraté, X.; Tomfohr, J.; Sankey, O. F.; Primak, A.; Moore, A. L.; Moore, T. A.; Gust, D.; Harris, G.; Lindsay, S. M. *Nanotechnology* **2002**, *13*, 5–14.

(24) Cui, X. D.; Primak, A.; Zaraté, X.; Tomfohr, J.; Sankey, O. F.; Moore, A. L.; Moore, T. A.; Gust, D.; Nagahara, L. A.; Lindsay, S. M. *J. Phys. Chem. B* **2002**, *106*, 8609–8614.

(25) Holmlin, R.; Haag, R.; Chabinc, M. L.; Ismagilov, R. F.; Cohen, A. E.; Terfort, A. Rampi, M. A.; Whitesides, G. M. *J. Am. Chem. Soc.* **2001**, *123*, 5075–5085.

(26) Rampi, M. A.; Whitesides, G. M. *Chem. Phys.* **2002**, *281*, 373–391.

(27) Slowinski, K.; Fong, H. K. Y.; Majda, M. *J. Am. Chem. Soc.* **1999**, *121*, 7257–7261.

(28) York, R. L.; Nguyen, P. T.; Slowinski, K. *J. Am. Chem. Soc.* **2003**, *125*, 5948–5953.

(29) Kushmerick, J. G.; Holt, D. B.; Pollack, S. K.; Ratner, M. A.; Yang, J. C.; Schull, T. L.; Naciri, J.; Moore, M. H.; Shashidhar, R. *J. Am. Chem. Soc.* **2002**, *124*, 10654–10655.

(30) Smalley, J. F.; Feldberg, S. W.; Chidsey, C. E. D.; Linford, M. R.; Newton, M. D.; Liu, Y. *J. Phys. Chem.* **1995**, *99*, 13141–13149.

(31) Weber, K.; Hockett, L.; Creager, S. J. *Phys. Chem. B* **1997**, *101*, 8286–8291.

(32) Slowinski, K.; Chamberlain, R. V.; Miller, C. J.; Majda, M. *J. Am. Chem. Soc.* **1997**, *119*, 11910–11919.

(33) Wang, W.; Lee, T.; Reed, M. A. *Phys. Rev. B* **2003**, *68*, 035416.

(34) Wang, W.; Lee, T.; Kretzschmar, I.; Reed, M. A. *Nano Lett.* **2004**, *4*, 643–646.

(35) Jaklevic, R. C.; Lambe, J. *Phys. Rev. Lett.* **1966**, *17*, 1139–1140.

(36) Lambe, J.; Jaklevic, R. C. *Phys. Rev.* **1968**, *165*, 821–832.

(37) Adkins, C. J.; Phillips, W. A. *J. Phys. C: Solid State Phys.* **1985**, *18*, 1313–1346.

(38) *Tunneling Spectroscopy: Capabilities, Applications, and New Techniques*; Hansma, P. K., Ed.; Plenum: New York, 1982.

(39) Stipe, B. C.; Rezaei, M. A.; Ho, W. *Science* **1998**, *280*, 1732–1735.

(40) Zhou, C.; Deshpande, M. R.; Reed, M. A.; Jones, L., II; Tour, J. M. *Appl. Phys. Lett.* **1997**, *71*, 611–613.

(41) (a) Chen, J.; Reed, M. A.; Rawlett, A. M.; Tour, J. M. *Science* **1999**, *286*, 1550–1552. (b) Chen, J.; Calvet, L. C.; Reed, M. A.; Carr, D. W.; Grubisha, D. S.; Bennett, D. W. *Chem. Phys. Lett.* **1999**, *313*, 741–748.

(42) Ralls, K. S.; Buhman, R. A.; Tiberio, R. C. *Appl. Phys. Lett.* **1989**, *55*, 2459–2461.

(43) Ethanol and alkane molecules were purchased from Sigma-Aldrich.

(44) Metzger, R. M.; Chen, B.; HoIpfer, U.; Lakshmikantham, M. V.; Vuillaume, D.; Kawai, T.; Wu, X.; Tachibana, H.; Hughes, T. V.; Sakurai, H.; Baldwin, J. W.; Hosch, C.; Cava, M. P.; Brehmer, L.; Ashwell, G. J. *J. Am. Chem. Soc.* **1997**, *119*, 10455–10466.

(45) Horowitz, P.; Hill, W. *The Art of Electronics*; Cambridge University Press: New York, 1989.

(46) Sze, S. M. *Physics of Semiconductor Devices*; Wiley: New York, 1981.

(47) (a) Thurstans, R. E.; Oxley, D. P. *J. Phys. D: Appl. Phys.* **2002**, *35*, 802–809. (b) Simmons, J. G.; Verderber, R. R. *Proc. R. Soc. London, Ser. A* **1967**, *301*, 77–102. (c) Dearnaley, G.; Stoneham, A. M.; Morgan, D. V. *Rep. Prog. Phys.* **1970**, *33*, 1129–1191.

(48) (a) Mann, B.; Kuhn, H. *J. Appl. Phys.* **1971**, *42*, 4398–4405. (b) Polymeropoulos, E. E.; Sagiv, J. *J. Chem. Phys.* **1978**, *69*, 1836–1847.

(49) Fan, F. F.; Yang, J.; Cai, L.; Price, D. W.; Dirk, S. M.; Kosynkin, D. V.; Yao, Y.; Rawlett, A. M.; Tour, J. M.; Bard, A. J. *J. Am. Chem. Soc.* **2002**, *124*, 5550–5560.

(50) Franz, W. In *Handbuch der Physik*; Flugge, S., Ed.; Springer-Verlag: Berlin, 1956; Vol. 17, p 155.

(51) (a) Lewicki, G.; Mead, C. A. *Phys. Rev. Lett.* **1966**, *16*, 939–941. (b) Stratton, R.; Lewicki, G.; Mead, C. A. *J. Phys. Chem. Solids* **1966**, *27*, 1599–1604. (c) Parker, G. H.; Mead, C. A. *Phys. Rev. Lett.* **1968**, *21*, 605–607.

(52) Brar, B.; Wilk, G. D.; Seabaugh, A. C. *Appl. Phys. Lett.* **1996**, *69*, 2728–2730.

(53) Joachim, C.; Magoga, M. *Chem. Phys.* **2002**, *281*, 347–352.

(54) Simmons, J. G. *J. Appl. Phys.* **1963**, *34*, 1793–1803.

(55) (a) Simmons, J. G. *J. Phys. D* **1971**, *4*, 613–657. (b) Maserjian, J.; Petersson, G. P. *Appl. Phys. Lett.* **1974**, *25*, 50–52.

(56) Tomfohr, J. K.; Sankey, O. F. *Phys. Rev. B* **2002**, *65*, 245105.

(57) (a) Yamamoto, H.; Waldeck, D. H. *J. Phys. Chem. B* **2002**, *106*, 7469–7473. (b) Napper, A. M.; Liu, H.; Waldeck, D. H. *J. Phys. Chem. B* **2001**, *105*, 7699–7707.

(58) Kaun, C.-C.; Guo, H. *Nano Lett.* **2003**, *3*, 1521–1525.

(59) Piccinin, S.; Selloni, A.; Scandolo, S.; Car, R.; Scoles, G. *J. Chem. Phys.* **2003**, *119*, 6729–6735.

(60) Bryant, M. A.; Pemberton, J. E. *J. Am. Chem. Soc.* **1991**, *113*, 8284–8293.

(61) Kato, H. S.; Noh, J.; Hara, M.; Kawai, M. *J. Phys. Chem. B* **2002**, *106*, 9655–9658.

(62) Castiglioni, C.; Gussoni, M.; Zerbi, G. *J. Chem. Phys.* **1991**, *95*, 7144–7149.

(63) The symbols  $\delta$ ,  $\gamma$ , and  $\nu$  denote in-plane rocking (r) and scissoring (s), out-of-plane wagging (w) and twisting (t), and stretching modes, respectively.

(64) (a) Molinari, M.; Rinnert, H.; Vergnat, M.; Weisbecker, P. *Mater. Sci. Eng., B* **2003**, *101*, 186. (b) Bogdanoff, P. D.; Fultz, B.; Rosenkranz, S. *Phys. Rev. B* **1999**, *60*, 3976–3981. (c) Mazur, U.; Hipps, K. W. *J. Phys. Chem.* **1982**, *86*, 2854–2860.

(65) (a) Mazur, U.; Hipps, K. W. *J. Phys. Chem.* **1981**, *85*, 2244–2249. (b) Kurata, H.; Hirose, M.; Osaka, Y. *Jpn. J. Appl. Phys.* **1981**, *20*, L811.

(66) Kushmerick, J. G.; Lazorcik, J.; Patterson, C. H.; Shashidhar, R.; Seferos, D. S.; Bazan, G. C. *Nano Lett.* **2004**, *4*, 639–642.

(67) Kirtley, J.; Hall, J. T. *Phys. Rev. B* **1980**, *22*, 848–856.

(68) Lauhon, I. J.; Ho, W. *Phys. Rev. B* **1999**, *60*, R8525–R8528.

(69) Klein, J.; Léger, A.; Belin, M.; Défourneau, D.; Sangster, M. J. L. *Phys. Rev. B* **1973**, *7*, 2336–2348.

(70) Lauhon, I. J.; Ho, W. *Rev. Sci. Instrum.* **2001**, *72*, 216–223.

(71) Kastner, M. A. *Phys. Today* **1993**, *January*, 24–31.

(72) *Molecular Electronics: Science and Technology*; Aviram, A., Ratner, M., Eds.; Annals of the New York Academy of Sciences; New York Academy of Sciences: New York, 1998; Vol. 852.

(73) Reimers, J.; Picconatto, C.; Ellenbogen, J.; Shashidhar, R. In *Molecular Electronics III*; Annals of the New York Academy of Sciences; Reimers, J. R., Picconatto, C. A., Ellenbogen, J. C., Shashidhar, R., Eds.; New York Academy of Sciences: New York, 2003; Vol. 1006.